Time-Dependent Kohn-Sham Electron Dynamics Coupled with Nonequilibrium Plasmonic Response via Atomistic Electromagnetic Model

Xunkun Huang, Wenshu Zhang, and WanZhen Liang[a)]
State Key Laboratory of Physical Chemistry of Solid Surfaces, Collaborative Innovation Center of Chemistry for Energy Materials, Fujian Provincial Key Laboratory of Theoretical and Computational Chemistry, and Department of Chemistry, College of Chemistry and Chemical Engineering, Xiamen University, Xiamen 361005, P. R. China.

Computational modeling of plasmon-mediated molecular photophysical and photochemical behaviours can help us better understand and tune the bound molecular properties and reactivity, and make better decisions to design and control nanostructures. However, computational investigations of coupled plasmon-molecule systems are challenging due to the lack of accurate and efficient protocols to evaluate these systems. Here we present a hybrid scheme by combining real time time-dependent density functional theory (RT-TDDFT) method with time-domain frequency dependent fluctuating charge (TD-ωFQ) model. At first, we transform ωFQ, which was formulated in the frequency domain, to time-domain and derive its equation-of-motion formulation. The TD-ωFQ introduces the nonequilibrium plasmonic response of metal nanoparticle (MNP) and atomistic interactions to the electronic excitation of QM region. Then we combine TD-ωFQ with RT-TDDFT. The derived RT-TDDFT/TD-ωFQ scheme allows us to effectively simulate the plasmon-mediated "real-time" electronic dynamics and even the coupled electron-nuclear dynamics by combining with the nuclear dynamics approaches. As a first application of the RT-TDDFT/TD-ωFQ method, we study the nonradiative decay rate and plasmon-enhanced absorption spectra of two small molecules in the proximity of sodium MNPs. Thanks to the atomistic nature of ωFQ model, the edge effect of MNP to absorption enhancement has also been investigated and unveiled.

I. INTRODUCTION

The plasmonic metal nanoparticles (PMNPs) support surface plasmon (SP), the collective oscillation of metal electron density. Under light irradiation with frequency that corresponds to the resonance energy of SP, the resonant photon induces a collective oscillation of conduction electrons of MNPs, then a phenomenon defined as localized SP resonance (LSPR) takes place. Because of the dramatic effect of LSPR, PMNPs have become an important component in many experimental settings, such as the surface-enhanced spectroscopy and plasmonic photocatalysts, in which PMNPs are used to control and manipulate light at the nanoscale, thus regulating the photophysical[1–6] and photochemical[7–12] behaviors of molecules in their vicinity by means of the complex interplay between the plasmon and molecular quantum transitions. To unravel the detailed interplay between the plasmon and molecules, it is essential to computationally model and simulate the light-PMNP-molecule system.

Ab initio modeling of the light-PMNP-molecule system remains highly challenging. Many hybrid quantum mechanics/classical mechanics or electrodynamics approaches have thus been developed to model the coupled systems, in which the molecule is described quantum-mechanically by the excited-state electronic structure approaches such as the time-dependent density functional theory (TDDFT), while the response of PMNPs are treated by classical electrodynamics methods,[13] such as Mie theory,[14] discrete dipole approximation (DDA),[15] finite difference time domain (FDTD),[16,17] and boundary element method (BEM).[18,19] However the continuum-dielectric assumption to MNPs becomes less appropriate for medium to small-sized particles, in which the effects of size, shape, and edge on the plasmonic response cannot be ignored.[20,21] Therefore, fully atomistic, yet classical, modeling of these MNPs is required to more accurately capture the plasmonic effect. Specifically, to account for the large polarizability of MNPs, (induced) charges, dipoles, and/or even multipoles would be introduced at each atom site, leading to several (polarizable) force field models for the plasmonic response of MNPs, including discrete interaction model (DIM),[22] frequency dependent fluctuating charge (ωFQ)[23,24] and fluctuating dipoles (ωFQFμ).[25]

The original ωFQ model, in which each metal atom is endowed with a charge varied as a response of the external electric field, was formulated in the frequency-domain, so that it can predict the plasmonic response of MNPs at certain frequencies. However, if one is interested in the (ultrafast) dynamics of the PMNPs or of the molecule absorbed to the PMNPs, the time-domain approach may provide an in-depth description.[26] Efforts on developing time-domain model have been made for BEM, polarizable continumm model (PCM), and MMPol by Corni's group [27–30], Li's group[31–34] and Wu et.al.[35] Inspired by ωFQ model, Yamada has developed a time-domain force-field method that incorporates the motion of free electrons, and it is thus able to perform molecular dynamics simulation for light-metal interaction.[36] In this work, we transform the atomistic model ωFQ into time-domain, and obtain the time-domain equation-of-motion (EOM) of fluctuating charges on metal atoms. To distinguish it with the original ωFQ, the later is called as TD-ωFQ. This provides an approach to study the temporal response of MNPs to arbitrary incident field, which would contain a large range of frequency components.

The atomistic classical models for MNPs, such as DIM and ωFQFμ, have been combined with QM to model the light-molecule-MNP system. Both QM/DIM[37–41] and

[a)]Electronic mail: liangwz@xmu.edu.cn

QM/ωFQFμ[42] were developed in frequency-domain. To effectively simulate the plasmon-mediated "real-time" electronic dynamics and even the coupled electron-nuclear dynamics by combining with the nuclear dynamics approaches, here we combine the TD-ωFQ with real-time TDDFT (RT-TDDFT) approach, and build the hybrid RT-TDDFT/TD-ωFQ approach. RT-TDDFT solves the time-dependent Kohn-Sham (TDKS) equations or EOM of the reduced density matrix directly in time domain,[43–48] and shows more advantage than linear response TDDFT on dealing with the excitation of much larger molecule and describing the "real-time" electron dynamics and even the coupled electron-nuclear dynamics by combining with the Ehrenfest or trajectory surface hopping with Tully's fewest-switches algorithm nuclear dynamics approaches.[49,50] The hybrid RT-TDDFT/TD-ωFQ method can describe the nonequilibrated dynamics when molecule and PMNP are in resonant, and the mutual interactions between excited molecules and PMNPs are treated at the atomistic level. In past decade, we have employed the hybrid RT-TDDFT/FDTD approach to simulate the plasmon-mediated molecular linear and nonlinear spectra[17,51] and plasmon-driven water-splitting reaction.[52] At that time, the polarization from the QM part to the classical part was ignored.

The rest of the article is organized as follows: In Sec. II, we derive the time-domain EOM of ωFQ and present how it couples to the TDKS equation. We also display the expression of molecular absorption cross section. In Sec. III A, we compare the calculated results by the time-domain ωFQ to its original frequency-domain formalism. Sec. III B focuses on the electron dynamics and absorption spectrum of HSiF molecule that is weakly coupled with Na_{1415} MNP. In Sec. III C, we investigate the edge effect and non-uniform near field at different sites of Na_{5083} MNP. Finally, the concluding remarks and the discussion of the limitations of RT-TDDFT/TD-ωFQ are summarized in Sec. IV.

II. METHODS

First, we briefly review the original formalism of ωFQ, and a brief comment on the physical meaning of the ωFQ equation can be found in Supporting Information (SI). For detailed derivation and discussion, readers can refer to Refs. 23,24, and Section S1 in SI. ωFQ method uses Drude's conduction model to describe the frequency response of a MNP, while it also includes the quantum tunneling effects. The fundamental equation of ωFQ is

$$(\mathbf{A} - z(\omega)\mathbf{I})\mathbf{q}(\omega) = \mathbf{R}(\omega), \tag{1}$$

where the elements of the real nonsymmetric matrix $\mathbf{A}$ read

$$A_{mn} = \sum_k \bar{K}_{mk}\left(T^{(0)}_{kn} - T^{(0)}_{mn}\right). \tag{2}$$

$\mathbf{T}^{(0)}$ is the charge-charge interaction kernel, and its expression is $\frac{1}{r_{mn}}\mathrm{erf}(\frac{r_{mn}}{R_{mn}})$ since the Gaussian charge model $q_m(\mathbf{r};\mathbf{r}_m) = q_m g_m(\mathbf{r};\mathbf{r}_m)$ is used to damp the electrostatic interaction between neighboring atoms. The Gaussian distribution is defined as

$$g_m(\mathbf{r};\mathbf{r}_m) = \frac{1}{\pi^{3/2}R_m^3}\exp\left(-\frac{|\mathbf{r}-\mathbf{r}_m|^2}{R_m^2}\right), \tag{3}$$

where R_m is the width of Gaussian functions, and $R_{mn} = \sqrt{R_m^2 + R_n^2}$. $\bar{\mathbf{K}}$ describes the exchange of charge between atoms, and its elements are

$$\bar{K}_{mn} = \begin{cases} (1 - f(r_{mn}))\dfrac{\mathscr{A}_{mn}}{r_{mn}}, & m \neq n, \\ 0, \quad \text{otherwise.} \end{cases} \tag{4}$$

The Fermi damping function $f(r_{mn})$ accounts for the quantum tunneling effects. $\mathscr{A}_{mn}$ is the effective area of charge exchange. The remaining terms in Eq.1 are correspondingly

$$z(\omega) = -\frac{i\omega + \tau\omega^2}{2\sigma_0}, \tag{5}$$

$$R_m(\omega) = \sum_n \bar{K}_{mn}\left(\varphi^{\mathrm{ext}}_m(\omega) - \varphi^{\mathrm{ext}}_n(\omega)\right), \tag{6}$$

where τ is mean free time, and σ_0 is the static conductivity of the metal material correspondingly. $\varphi^{\mathrm{ext}}_m(\omega)$ is the electric potential felt by atom m. In one word, $\mathbf{R}(\omega)$ is the external driven force that causes charge exchange and fluctuation; $\mathbf{A}$ describes the charge equilibrium between atoms; and $z(\omega)$ describes the mobility of electrons. In the presence of external field $\mathbf{E}^{\mathrm{ext}}(\omega)$ with frequency ω, $\varphi^{\mathrm{ext}}_m(\mathbf{r},\omega) = -\mathbf{r}_m \cdot \mathbf{E}^{\mathrm{ext}}(\omega)$ in the long-wavelength approximation, then the frequency-dependent induced charge of metal atoms $\mathbf{q}(\omega)$ are obtained by solving Eq.1.

A. ωFQ in Time Domain

The extension of ωFQ to time-domain is straightforward. We expand Eq.1 as following

$$\tau\omega^2\mathbf{q}(\omega) + i\omega\mathbf{q}(\omega) = 2\sigma_0[-\mathbf{A}\mathbf{q}(\omega) + \mathbf{R}(\omega)], \tag{7}$$

and apply inverse Fourier transform (FT) on both sides. Note that due to the property of FT $\mathscr{F}\left[\frac{\mathrm{d}^n}{\mathrm{d}t^n}q(t)\right] = (-i\omega)^n q(\omega)$, the equation-of-motion (EOM) of charges in time-domain is

$$\frac{\mathrm{d}^2\mathbf{q}}{\mathrm{d}t^2} + \frac{1}{\tau}\frac{\mathrm{d}\mathbf{q}}{\mathrm{d}t} = \frac{2\sigma_0}{\tau}[\mathbf{A}\mathbf{q}(t) - \mathbf{R}(t)]. \tag{8}$$

It is clear that the EOM describes the induced charges as forced damped harmonic oscillators. The leapfrog method is adopted to numerically integrating Eq.8.[53] To do so, we define

$$\mathbf{J}(t) = \frac{\mathrm{d}\mathbf{q}}{\mathrm{d}t}, \tag{9}$$

so that the EOM of $\mathbf{J}$ is

$$\frac{\mathrm{d}\mathbf{J}}{\mathrm{d}t} = -\frac{1}{\tau}\mathbf{J} + \frac{2\sigma_0}{\tau}[\mathbf{A}\mathbf{q}(t) - \mathbf{R}(t)]. \tag{10}$$

Therefore the evolution equations for $\mathbf{q}$ and $\mathbf{J}$ are

$$\mathbf{q}(t_i + \mathrm{d}t) = \mathbf{q}(t_i) + \mathbf{J}(t_i + \mathrm{d}t/2)\mathrm{d}t, \tag{11}$$

$$\mathbf{J}(t_i + \mathrm{d}t/2) = \frac{2\tau - \mathrm{d}t}{2\tau + \mathrm{d}t}\mathbf{J}(t_i - \mathrm{d}t/2) + \frac{4\sigma_0 \mathrm{d}t}{2\tau + \mathrm{d}t}[\mathbf{A}\mathbf{q}(t_i) - \mathbf{R}(t_i)]. \tag{12}$$

The detailed derivation is shown in Section S1.3 in SI. The initial values of $\mathbf{q}$ and $\mathbf{J}$ are zero. The time-dependent induced charges $\mathbf{q}(t)$ are updated via the Eq.11 as time-dependent external field $\mathbf{E}^{\mathrm{ext}}(t)$ is applied to the MNP.

In addition, as can be seen in Eq.8, the spectral broadening of ωFQ is determined by $1/\tau$, and the response frequency is determined by metal electron density $n = \sigma_0/\tau$. Because the current ωFQ does not incorporate the effect of the relaxation processes, for example, surface scattering of the limited sized PMNPs, the only way to include the spectral broadening mechanism is artificially scale the value of τ (and of σ_0 simultaneously so that the absorption peaks will not shift). This point has already been discussed in the supporting information of Ref. 23. Since the spectral broadening is related to the decay rate of time-dependent response, the effect of scaling parameters should also emerges in the time-domain ωFQ results. In this work, the choice of scaling factor is rationalized in the SI, where the fitting equations are presented for sodium MNP and nanorod.

B. ωFQ Coupled with QM Hamiltonian

One can combine ωFQ and QM method to study the system that is composed by an absorbed molecule and the plasmonic material. The ground state of such a composed system without external electric field is described by the QM/Fluctuating Charge (FQ) method,[54–56] in which the equilibrium of polarization of both QM part and FQ part is achieved when SCF is converged. The ground state Fock matrix in atomic orbital basis (AO) is

$$\mathbf{F} = \mathbf{h} + \mathbf{G}(\mathbf{P}) + \mathbf{V}^{\dagger}\mathbf{q}(\mathbf{P}), \tag{13}$$

where $\mathbf{h}$ is the core Hamiltonian including nuclear-electron attraction and electron kinetic energy terms, and $\mathbf{G}(\mathbf{P}) = \Pi \cdot \mathbf{P} + \mathbf{F}^{\mathrm{XC}}(\mathbf{P})$. The two-electron integral supermatrix Π in atomic basis is $\Pi_{\mu\nu,\lambda\sigma} = (\mu\nu|\lambda\sigma) - c_{\mathrm{HFX}}(\mu\lambda|f(\vec{r}_{12})|\nu\sigma)$, adopting approximate coefficient c_{HFX} and operator $f(\vec{r}_{12})$ for hybrid and range-separated functionals. $\mathbf{F}^{\mathrm{XC}}$ is exchange-correlation (XC) potential. The fluctuating charges $\mathbf{q}$ are obtained by solving FQ equation (shown in SI), and they depend on the density matrix implicitly because a part of them is induced by electrons' charge density. $\mathbf{V}$ describes the interaction between fluctuating charges and electrons, and its elements are

$$V_{m,\mu\nu} = -\int \chi_\mu(\mathbf{r}') \frac{g_m(\mathbf{r};\mathbf{r}_m)}{|\mathbf{r} - \mathbf{r}'|} \chi_\nu(\mathbf{r}')\, \mathrm{d}\mathbf{r}\mathrm{d}\mathbf{r}'. \tag{14}$$

The Gaussian distribution $g_m(\mathbf{r};\mathbf{r}_m)$ is presented in Eq.3 and it serves as a $1s$ orbital. Therefore Eq. 14 is a three-center-two-electron integral.

If time-dependent electric field is applied on the equilibrated composed system, the electron density of the QM molecule is induced to change under the influence from both external field and local field produced by the PMNP. We use RT-TDDFT method to describe the time evolution of QM part, and the evolution of PMNP is calculated via TD-ωFQ. In the generalized nonorthogonal AO basis sets, the EOM of reduced density matrix is expressed as[45,57]

$$i\frac{\partial \mathbf{P}(t)}{\partial t} = \mathbf{S}^{-1}\mathbf{F}\mathbf{P} - \mathbf{P}\mathbf{F}\mathbf{S}^{-1} - i\gamma[\mathbf{P}(t) - \mathbf{P}(0)], \tag{15}$$

where $\mathbf{S}$ is the overlap matrix. The third term in the right-hand-side of TDKS equation is a phenomenological description of damping of density matrix where γ represents damping rate. The concrete form of the dissipation term and the numerical integration method to solve TDKS equation are discussed in Appendix A.

The time-dependent Fock matrix is

$$\mathbf{F}(t) = \mathbf{F}_0(\mathbf{P}(t)) - \mathbf{M} \cdot \vec{E}^{\mathrm{ext}}(t) + \mathbf{V}^{\dagger}\mathbf{q}^{\mathrm{sca}}(t) + \mathbf{V}^{\dagger}\mathbf{q}^{\mathrm{pol}}(t). \tag{16}$$

In this work, adiabatic approximation is adopted so that the XC functional is just the ground state one. We would emphasize that the ground state fluctuating charges $\mathbf{q}_0$ have been set frozen in $\mathbf{F}_0$, that is, only the two-electron term is time-dependent:

$$\mathbf{F}_0(\mathbf{P}(t)) = \mathbf{h} + \mathbf{G}(\mathbf{P}(t)) + \mathbf{V}^{\dagger}\mathbf{q}_0. \tag{17}$$

$\mathbf{M}$ is the dipole matrix. The time-dependent fluctuating charges are made up of two parts, $\mathbf{q}^{\mathrm{sca}}(t)$ and $\mathbf{q}^{\mathrm{pol}}(t)$, and their evolution follows Eq.11 under corresponding potentials. $\mathbf{q}^{\mathrm{sca}}(t)$ is directly induced by external field $\mathbf{E}^{\mathrm{ext}}(t)$, which attributes to the "near field effects" proposed by Jensen.[38] $\mathbf{q}^{\mathrm{pol}}(t)$ stems from the induced charge density, more precisely, the induced electric potential of QM molecule, and can be thought as the "image field". The QM electric potential acting on the atom m of MNP can be calculated in the AO basis

$$\delta\varphi_m^{\mathrm{QM}}(t) = \sum_{\mu\nu} \delta P_{\mu\nu}(t) V_{m,\mu\nu}. \tag{18}$$

In conclusion, in our RT-TDDFT/TD-ωFQ computation, the MNP experiences the actions from two sources: external field $\mathbf{E}^{\mathrm{ext}}(t)$ and QM induced electric potential $\delta\varphi^{\mathrm{QM}}(t)$. Two groups of polarization charges $\mathbf{q}^{\mathrm{sca}}(t)$ and $\mathbf{q}^{\mathrm{pol}}(t)$ are induced respectively under these two sources. Then the charges $\mathbf{q}^{\mathrm{sca}}(t)$ and $\mathbf{q}^{\mathrm{pol}}(t)$ of MNP, plus external field $\mathbf{E}^{\mathrm{ext}}(t)$, serve as time-dependent perturbations to QM molecule as described by Eq. 16.

C. The Absorption Cross Section of the Molecule in the Proximity of MNPs

When a molecule is in the proximity of MNPs, the field acting on the molecule which interacts with MNPs includes the incident laser field and the scattered field produced by the

MNPs. Therefore the light absorption of QM molecule includes two parts of contributions, and the corresponding absorption cross section can be written as[29]

$$\sigma(\omega) = \frac{4\pi\omega}{c} \frac{\mathrm{Im}\left[\int \mathrm{d}\mathbf{r}\, \delta\rho^*(\mathbf{r},\omega)\varphi^{\mathrm{tot}}(\mathbf{r},\omega)\right]}{\left|\mathbf{E}^{\mathrm{ext}}(\omega)\right|^2}. \tag{19}$$

Here $\delta\rho(\mathbf{r},\omega)$ is the charge density of QM molecule induced by $\varphi^{\mathrm{tot}}(\mathbf{r},\omega)$, which is composed of two terms, $\varphi^{\mathrm{ext}}(\mathbf{r},\omega) + \varphi^{\mathrm{sca}}(\mathbf{r},\omega)$. The first one is external electric potential and the second is the potential arisen by the scattered field of MNPs. The contribution of image potential φ^{pol} or q^{pol} has been neglected by assuming that it's contribution is small. With respect to the partition of $\varphi^{\mathrm{tot}}(\mathbf{r},\omega)$, we then divide this absorption cross section into two parts $\sigma^{\mathrm{ext}} + \sigma^{\mathrm{sca}}$. In the first term, as long-wavelength approximation is applied, $\varphi^{\mathrm{ext}}(\mathbf{r},\omega) = -\mathbf{r}\cdot\mathbf{E}^{\mathrm{ext}}(\omega)$, and

$$\sigma^{\mathrm{ext}}(\omega) = -\frac{4\pi\omega}{c} \frac{\mathrm{Im}\left[\delta\mu^*(\omega)\cdot\mathbf{E}^{\mathrm{ext}}(\omega)\right]}{\left|\mathbf{E}^{\mathrm{ext}}(\omega)\right|^2}, \tag{20}$$

where $\delta\mu(\omega)$ is induced electric dipole in the frequency domain

$$\delta\mu(\omega) = \int \mathbf{r}\delta\rho(\mathbf{r},\omega)\,\mathrm{d}\mathbf{r}. \tag{21}$$

The potential of scattered near field can be calculated via the fluctuating charges

$$\varphi^{\mathrm{sca}}(\mathbf{r},\omega) = \sum_m \int \frac{q_m^{\mathrm{sca}}(\omega) g_m(\mathbf{r}';\mathbf{r}_m)}{|\mathbf{r}-\mathbf{r}'|}\,\mathrm{d}\mathbf{r}', \tag{22}$$

and $\delta\rho(\mathbf{r},\omega)$ can be calculated by

$$\delta\rho(\mathbf{r},\omega) = -\sum_{\mu\nu} \delta P_{\nu\mu}(\omega)\chi_\mu^*(\mathbf{r})\chi_\nu(\mathbf{r}). \tag{23}$$

Then the second term in cross section is

$$\begin{aligned}\sigma^{\mathrm{sca}}(\omega) &= \frac{4\pi\omega}{c} \frac{\mathrm{Im}\left[\sum_m \sum_{\mu\nu} \delta P_{\mu\nu}^*(\omega) V_{m,\mu\nu} q_m^{\mathrm{sca}}(\omega)\right]}{\left|\mathbf{E}^{\mathrm{ext}}(\omega)\right|^2} \\ &= \frac{4\pi\omega}{c} \frac{\mathrm{Im}\left[\sum_m \delta\varphi_m^{\mathrm{ele}*}(\omega) q_m^{\mathrm{sca}}(\omega)\right]}{\left|\mathbf{E}^{\mathrm{ext}}(\omega)\right|^2}.\end{aligned} \tag{24}$$

In the above context, $\delta\mu(\omega)$ and $\mathbf{E}^{\mathrm{ext}}(\omega)$ are obtained via the fast Fourier transform (FFT) of $\delta\mu(t)$ and $\mathbf{E}^{\mathrm{ext}}(t)$ respectively. However, for $\delta\varphi_m^{\mathrm{ele}}(\omega)$ and $q_m^{\mathrm{sca}}(\omega)$, they are calculated directly via the numerical integration during the propagation of RT-TDDFT simulation

$$\delta\varphi_m^{\mathrm{ele}}(\omega) = \int_0^{t_{\max}} \delta\varphi_m^{\mathrm{ele}}(t) \mathrm{e}^{i\omega t}\,\mathrm{d}t, \tag{25}$$

$$q_m^{\mathrm{sca}}(\omega) = \int_0^{t_{\max}} q_m^{\mathrm{sca}}(t) \mathrm{e}^{i\omega t}\,\mathrm{d}t. \tag{26}$$

Otherwise, one would have to save all data of $\delta\varphi_m^{\mathrm{ele}}(t)$ and $q_m^{\mathrm{sca}}(t)$ in disk, which is slow and requires a lot of storage space.

On the other hand, for MNP, we calculate its absorption cross section in normal way, i.e.

$$\frac{4\pi\omega}{c}\mathrm{Im}\left[\frac{\delta\boldsymbol{\mu}^{\mathrm{MNP}}(\omega)}{\mathbf{E}^{\mathrm{ext}}(\omega)}\right], \tag{27}$$

where the total induced dipole of MNP is $\delta\boldsymbol{\mu}^{\mathrm{MNP}}(\omega) = \sum_m \mathbf{r}_m\left[q_m^{\mathrm{sca}}(\omega) + q_m^{\mathrm{pol}}(\omega)\right]$. The reasons why we calculate the dipole of MNP this way include both theoretical and technical aspects. We would assume that the molecular dipole induced by the incident external electric field is relatively small, and normally it is difficult to single out the direct response term of a molecule from its density matrix $\mathbf{P}(t)$.

III. RESULTS

The ωFQ is first implemented as standalone C++ code, then its time-domain formalism is added into a development version of Q-Chem package[58] to be coupled with TDKS module. The values of parameters of ωFQ used in this work are listed in Section S2 in SI. The undamped TDKS implementation (including various time propagation algorithm) in Q-Chem was developed by Zhu et al.[59,60] We add the dissipation propagator on the basis of their implementation.

The molecular coordinates of HSiF come from Ref. 61, and the geometry of BODIPY is optimized at the theoretical level of B3LYP[62]/def2-SVP[63]. The structures of sodium nanoparticles and nanorods are generated using the Atomic Simulation Environment (ASE) Python module.[64] Because ωFQ does not account for the plasmon response of d-electron, which is significant for the plasmonic metal like gold and silver, in this work we only consider sodium MNPs. The RT-TDDFT/TD-ωFQ method does not consider the charge transfer between the molecule and the MNP, so in all the examples we show, the nearest distance between the molecule and the MNP's surface is at least 5 Å.

A. Validation of TD-ωFQ

Since the TD-ωFQ is directly derived from its original frequency-domain formalism via Fourier transform, one would expect that they produce equivalent results given the same set of parameters. Here we select a sodium nanorod containing 515 atoms (the longitudinal length is about 60 Å) to calculate its absorption spectrum. The longitudinal axis of nanorod is parallel to z-axis. For frequency-domain ωFQ, we scan the frequency of the perturbing harmonic electric field which is z-polarized, and solve the dipolar response $\delta\mu_z(\omega)$ of nanorod at the corresponding frequency

$$\delta\mu_z(\omega) = \sum_m r_{m,z} q_m^{\mathrm{sca}}(\omega). \tag{28}$$

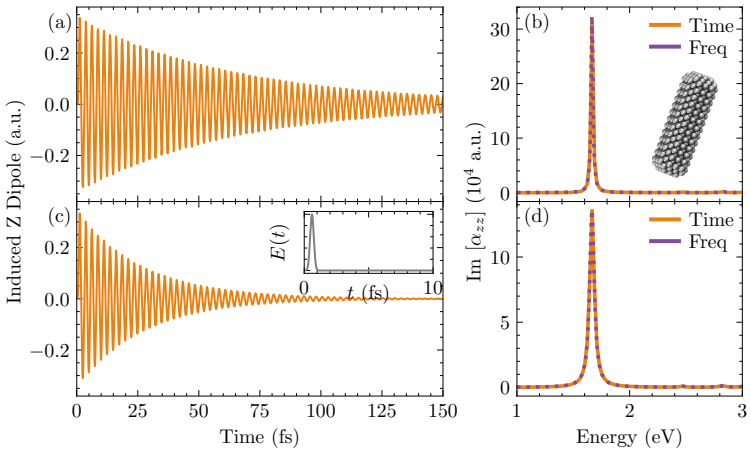

FIG. 1. Comparison of results calculated by the time-domain and frequency-domain ωFQ for a sodium nanorod. The upper parts are calculated using unscaled parameters and lower parts are those with the parameters scaled by a scaling factor of 0.415.

Then the frequency-dependent polarizability is calculated via the simple expression

$$\alpha_{zz}(\omega) = \frac{\delta\mu_z(\omega)}{E_z^{\text{ext}}(\omega)}. \tag{29}$$

As shown in Fig. 1(b), the unchanged σ_0 and τ give a sharp absorption peak near 1.73 eV. And if we scale the value of σ_0 and τ by 0.415, which is given by our fitting formula, the full width at half maximum (FWHM) of spectral peak slightly increases, as illustrated in Fig. 1(d).

In TD-ωFQ calculation, we apply a narrow Gaussian wavepacket form of electric field, $E(t) = \exp[-(t-t_0)^2/2\sigma^2]$ where $t_0 = 0.6$ fs and $\sigma = 0.14$ fs. The time-variant induced dipole $\delta\mu_z(t)$ at each step of propagation is calculated. The time step of simulation is set to be 0.1 a.u.. Then we apply FFT for both external field and induced dipole to obtain their frequency-domain values, and calculate the frequency-dependent polarizability. From Fig. 1(b) and (d), it is clear that the profiles of the imaginary part of polarizability from frequency-domain and time-domain ωFQ are well superposed, which validates the correctness of time-domain implementation. The time-dependent induced dipoles without and with scaling are plotted in Fig. 1(a) and (c) respectively. Comparing these two situations, one can find that the scaling of parameters can change the decay rate of induced dipoles, which may bring important influence to the dynamics of PMNP/absorbed molecule system.

B. The Absorption Spectrum of HSiF

The first example is the HSiF molecule absorbed on the icosahedral Na_{1415} nanoparticle. HSiF is a closed-shell small molecule and its main low-energy absorption peak located at around 3.0 eV perfectly overlaps with that of plasmonic resonance excitation of Na_{1415}. The geometric configuration of HSiF/Na_{1415} is shown in Fig. 2(a). They are stacked along the z-direction (the plane of HSiF is perpendicular to z-axis), and

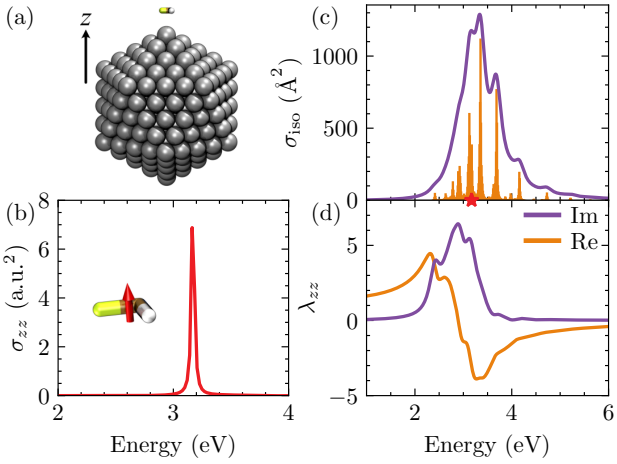

FIG. 2. (a) A depiction of the HSiF/Na_{1415} system. (b) The absorption spectrum and $S_0 \rightarrow S_1$ transition dipole of isolated HSiF. (c) Absorption and (d) field enhancement spectrum of Na_{1415}

.

the distance between the center of mass (COM) of HSiF and the closed Na atom is 5 Å. All ωFQ results for Na_{1415} in this section are calculated using the scaling factor of 0.0786 as the radius of nanoparticle is about 21.9 Å.

We first calculate the absorption spectrum of an isolated HSiF molecule using RT-TDDFT at the HF/def2-SVPD[65] level of theory, and only the transition along the z-direction is considered. The time step of RT-TDDFT propagation is 0.02 a.u. (0.48 as), and the total time of simulation is 190 fs. The damping rate $\gamma_0 = 5 \times 10^{-4}$ a.u. (0.003 fs^{-1}) is used to represent vibrational relaxation. The calculated excitation energy of S_1 state is 3.1704 eV which is close to the reference result 3.07 eV at CC3/aug-cc-pVTZ level.[61]

The response properties of a single Na_{1415} MNP which are calculated via frequency-domain ωFQ are also presented. In Fig. 2(c), the lineshape of isotropic absorption spectrum is plotted. The vertical lines are transitions calculated using

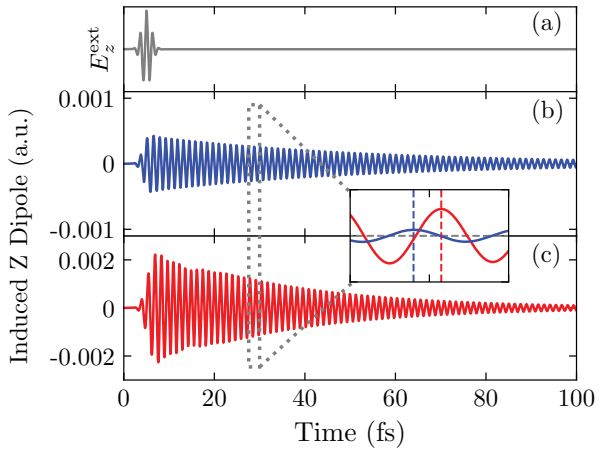

FIG. 3. The induced dipoles of HSiF in (b) isolated case and (b) near the PMNP due to an external field (a).

the unscaled parameters. It is obvious that the absorption of Na_{1415} covers a wide range of energy. The most intense transition occurs at the frequency of 3.35 eV, and a slightly lower peak is at 3.19 eV. The absorption peak of HSiF is superposed with the absorption of Na_{1415} as hinted by the star marker. We also study the electric field enhancement of Na_{1415} by applying a uniform field along the z-direction and calculate the scattered field at the COM of HSiF. The enhancement is characterized by the following quantity

$$\lambda_{zz}(\omega) = \frac{E_z^{\mathrm{sca}}(\omega)}{E_z^{\mathrm{ext}}(\omega)}. \tag{30}$$

The λ_{zz} of Na_{1415} is plotted in Fig. 2(d) including both real part and imaginary part. Unlike absorption spectrum, the field enhancement is stronger for low energy transitions than for higher energy transitions, because the scattered field generated by the former transitions is localized on the vertex of MNP, while the scattered field of the latter tends to be limited within the volume of MNP.[66–68]

Then the composite system of HSiF/Na_{1415} is studied using hybrid RT-TDDFT/TD-ωFQ method. An incident field of Gaussian envelope style $\mathbf{E}^{\mathrm{ext}}(t) = \mathbf{E}_0^{\mathrm{ext}} \exp[-(t-t_0)^2/2\sigma^2]\cos[\omega_0(t-t_0)]$ is applied to excite this system. The polarization direction of field vector $\mathbf{E}_0$ is z-direction and its magnitude is 1×10^{-5} a.u.. The central frequency ω_0 of field is 3 eV. $t_0 = 5$ fs and $\sigma = 1.03$ fs where the latter corresponds to FWHM of 1.5 eV in frequency domain. The settings for RT-TDDFT simulation are identical to the isolated HSiF described in the above context. Fig. 3 shows the induced dipoles of an isolated HSiF molecule and the one near the PMNP. There are three points worth discussing. First, one can easily find that when HSiF is absorbed on MNPs, the maximum amplitude of the induced dipole is approximately 5 times larger than that in isolated system. This result is straightforward since Na_{1415} nanoparticle produces enhanced near field at the position of HSiF. The second difference is the decay rate of induced dipole. For the isolated case, the envelope of induced dipole exhibits exponential decay, and we obtain the decay rate by fitting. The fitted value of rate is 5×10^{-4} a.u., and it is equal to γ_0 we have set in advance, which validates our implementation of dissipation propagator. In contrast, when HSiF is close to a MNP, its decay rate is 8.104×10^{-4} a.u. (0.005 fs^{-1}). This means that the presence of MNP enables a new energy relaxation pathway whose decay rate is 3.104×10^{-4} a.u.. The last point is the phase shift of temporal induced dipoles due to exciton-plasmon interaction. In this example, the phase shift is about $\pi/2$, and we will see later that it can cause interference pattern in spectral lines.

The extra nonradiative decay is due to the energy transfer from HSiF to Na_{1415}.[69] In the frequency domain, the expression of rate is[70–72]

$$\gamma_\rho = -\sum_m \mathrm{Im}[q_m(\rho_{\mathrm{eg}})]\varphi(\mathbf{r}_m, \rho_{\mathrm{eg}}). \tag{31}$$

$q_m(\rho_{\mathrm{eg}})$ is the fluctuating charge induced by molecular transition density ρ_{eg} at the transition frequency, and $\varphi(\mathbf{r}_m, \rho_{\mathrm{eg}})$ is the electric potential generated by ρ_{eg} at the position of charge q_m. On the other hand, in the commonly used point-dipole approximation, the rate is expressed using electric transition dipole moment μ_{eg} instead

$$\gamma_\mu = \mathrm{Im}[\mathbf{E}(\mu_{\mathrm{eg}})]\cdot\mu_{\mathrm{eg}}, \tag{32}$$

where $\mathbf{E}(\mu_{\mathrm{eg}})$ is the scattered field of PMNP induced by μ_{eg}.

Within the frequency range we study, HSiF is excited to its S_1 states. To calculate the decay rate from the frequency-domain perspective, the transition density and transition dipole moment of S_1 states are obtained from the linear response calculation of an isolated HSiF at the same level of theory. For transition density, the result is $\gamma_\rho = 3.139\times10^{-4}$ a.u., and for transition dipole moment, $\gamma_\mu = 2.734\times10^{-4}$ a.u.. We find both expressions match well with the RT-TDDFT/TD-ωFQ results, however the rate calculated via transition density is closer. It can be seen that the deviation of point-dipole approximation from the atomistic description exists even for small molecule.

In Fig. 5, we show the overall absorption spectrum of HSiF. It is partitioned into two terms σ^{ext} and σ^{sca}, which are interpreted as energy dissipation from the external field and the scattered near field, respectively. The profile of σ^{ext} shows asymmetric lineshape. This is the result of the phase shift of dipoles.[73] The main contribution of optical absorption is from σ^{sca}. A shown in panel (b), the spectral line of σ^{sca} features a peak with great magnitude and a shallow dip on the left of that peak. The total absorption spectrum of HSiF absorbed on Na_{1415} is the combination of the above two parts. It is clear that the optical absorption of HSiF is largely enhanced for about 25 times comparing to the isolated one. And slight blue shift is observed in the absorption peak which also reflects the interaction between excited HSiF and plasmonic Na_{1415}.

We could also look into the absorption spectrum of Na_{1415} in the interacting system. The total response of Na_{1415} also consists of two terms, $\mathbf{q}^{\mathrm{sca}}$ due to external field and $\mathbf{q}^{\mathrm{pol}}$ due to excited molecule, and their corresponding dipoles are plotted

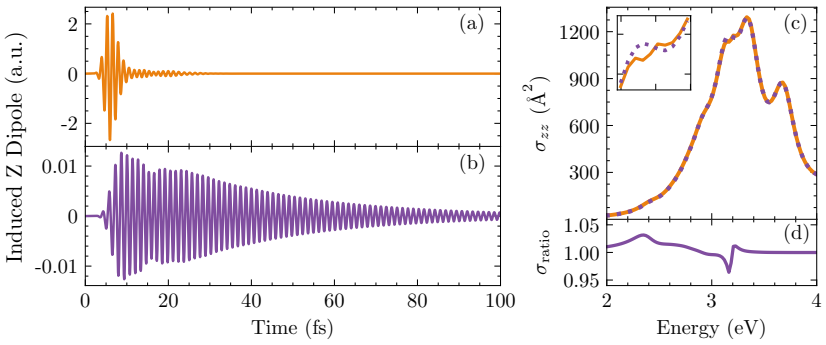

FIG. 4. The induced dipoles of Na_{1415} in the HSiF/Na_{1415} composite system: (a) induced by external field, (b) induced by HSiF. (c) The total absorption of Na_{1415} in composite system is plotted in solid line, and the absorption of isolated Na_{1415} is plotted in dotted line for comparison. (d) The spectral ratio $\sigma_{\rm ratio} = \sigma/\sigma_{\rm iso}$.

in Fig. 4(a) and (b). The total absorption cross section is plotted as the solid line in Fig. 4(c). For comparison, the cross section of isolated Na_{1415} (which is directly derived from the $\mathbf{q}^{\rm sca}$ part of dipoles) is drawn in dotted line. Since the perturbation from the nearby exciton is weak, the spectral line of MNP does not show significant changes. To clearly resolve the detailed change in lineshape, we define the spectral ratio $\sigma_{\rm ratio} = \sigma/\sigma_{\rm iso}$, and plot it in the (d) panel of Fig. 4. The asymmetric interference pattern at the HSiF excitation frequency and the weak enhancement around 2.4 eV emerge in the spectral line, and they are ascribed to the exciton-plasmon coupling.[74,75]

C. The Absorption Spectrum of BODIPY

To show the edge effect of MNP, in this section we present a brief example made up of BODIPY and Na_{5083} icosahedral MNP. The DFT XC functional and basis set used for BODIPY are B3LYP and def2-SVP, respectively. The decay rate is set 1×10^{-3} a.u. (0.007 fs^{-1}) for RT-TDDFT, and the scaling factor 0.118 is adopted in ωFQ part. The excited states of BODIPY involved in the exciton-plasmon interaction include S_1 (3.19 eV) and S_2 (3.69 eV), and their corresponding transition dipoles are shown in Fig. 6. Both transition dipoles are aligned along the long axis of BODIPY.

We consider two configurations: BODIPY close to the edge

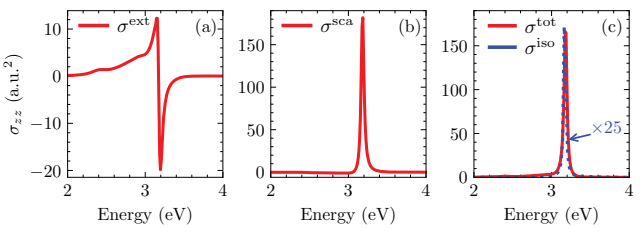

FIG. 5. The absorption spectrum of HSiF absorbed on Na_{1415}. The total cross section $\sigma^{\rm tot}$ in (c) is the summation of (a) $\sigma^{\rm ext}$ and (b) $\sigma^{\rm sca}$. The cross section of isolated HSiF is also plotted in (c) for comparison where its value is scaled by 25 for clarity.

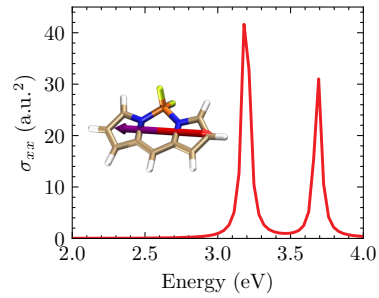

FIG. 6. The absorption spectra of isolated BODIPY. The red and blue arrows denote $S_0 \rightarrow S_1$ and $S_0 \rightarrow S_2$ transition dipoles, respectively.

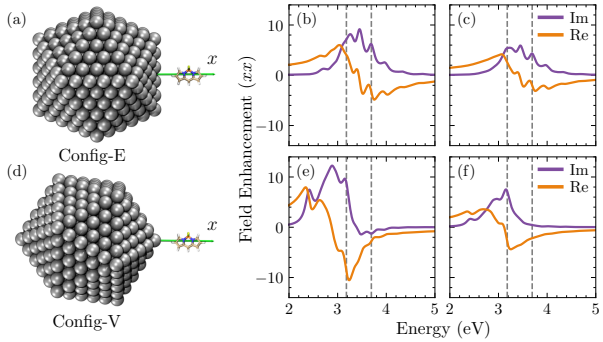

FIG. 7. Depictions of (a) **E**dge-configuration and (d) **V**ertex-configuration of BODIPY/Na_{5083} where the closest distance between BODIPY and Na_{5083} is 5 Å. Field enhancement spectrum of **E**-configuration at (b) the point of 5 Å away from the boundary of MNP, and (c) the COM of BODIPY. Field enhancement spectrum of **V**-configuration at (e) the point of 5 Å away from the boundary of MNP, and (f) the COM of BODIPY.

(**E**) and the vertex (**V**) of Na_{5083}. In both configurations, the long axis of BODIPY is parallel to the x-axis, and BODIPY approaches MNP along the x-axis. Fig.7 (a) and (d) denote the **E**- and **V**-configuration with the closest distance being 5 Å, in which the distance is defined as the separation between the leftmost H atom of BODIPY and the MNP boundary.

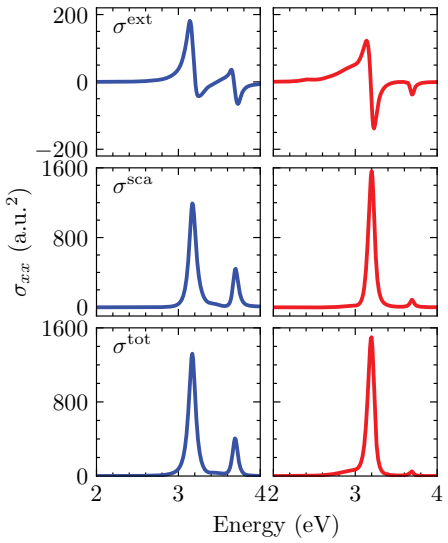

FIG. 8. The absorption spectra of BODIPY absorbed on the edge of Na_{5083} (left column) and on the vertex of Na_{5083} (right column).

The enhanced absorption spectra of BODIPY in two configurations computed by RT-TDDFT/TD-ωFQ method are displayed in the left and right columns of Fig.8, respectively. For **E**-configuration, the asymmetric line shape appears at both S_1 and S_2 excitation frequencies in σ^{ext} term. In contrast, since the phase delay of near field is equal to π, σ^{ext} of **V**-configuration has a interference dip at S_2 excitation frequency. The line-shapes of σ^{sca} and σ^{tot} in two configurations are quite different: both S_1 and S_2 absorption peaks are effectively enhanced in **E**-configuration, while only S_1 peak is conspicuous in **V**-configuration.

To explain the above different enhancement behavior exhibited in the absorption spectra, we calculated the the field enhancement factors at two points for both **E**- and **V**- configurations (assuming the uniform external electric field is applied along x-direction). Both points lie on the x-axis, and the first one lies in the location of the closest H atom (5 Å away from the boundary of MNP), while the further point is on the COM of BODIPY (about 9.45 Å from the boundary). As Fig.7 shows, the field enhancement factors are very much dependent on the molecular locations. The larger is the surface separation, the smaller is the field enhancement. The near field shows the well-known non-uniform characteristics. In **E**-configuration, the most intense near field generated at the edge of MNP covers the excitation frequencies of BODIPY S_1 and S_2 states, of which the excitation frequencies are presented by the dashed lines as shown in Fig.7 (b) and (c). Comparing the spectral lines at two points, near field at the edge of MNP attenuates as the distance increases, showing its non-uniform characteristics, and the overall shape of spectral lines change slightly. The field enhancement spectra of **V**-configuration, plotted in Fig.7 (e) and (f), show different traits. The maximum value of near field is greater and emerges at lower frequencies in **V**-configuration case. Therefore only the S_1 absorption of BODIPY is effectively enhanced. And from 5 Å to 9.45 Å, those near field localized on the vertex attenuates dramatically.

IV. CONCLUDING REMARKS

In this work, we propose the hybrid RT-TDDFT/TD-ωFQ method for the description of electron dynamics and the calculation of absorption spectrum of the molecule-PMNP coupled system. We transform the original ωFQ method derived in frequency domain to time domain, in which the system of linear equations is replaced by the equation-of-motion. The time-domain formalism of ωFQ allows us to calculate the real-time response of PMNPs. At fist, the correctness of TD-ωFQ is demonstrated by the comparison between the results yielded by the frequency-domain and time-domain ωFQ. In the RT-TDDFT part, we use the language of orbital rotation to derive the specific form of the dissipation term. With the addition of dissipative propagator, we can include dissipation *in situ* in the RT-TDDFT simulation, although phenomenologically, instead of artificially applying damping function after the calculations.

The RT-TDDFT/TD-ωFQ method is firstly applied to the weakly coupled HSiF/Na_{1415} system. In this case, the inclusion of exciton-plasmon interaction leads to the additional pathway of nonradiative energy transfer in the electron dynamics of exciton. Enhancement of molecular absorption spectrum and Fano asymmetric interference pattern are also observed in our simulation. In the BODIPY/Na_{5083} example, we investigate the edge effect of the MNPs. The plasmon near fields that localized on the edge and vertex of MNP have different field gradients, and show different performance of enhancing the absorption spectrum of the nearby molecule. Our RT-TDDFT/TD-ωFQ method provides a useful and affordable tool to study the electron dynamics of the light-molecule-PMNP system. It may also be feasible for exploring strongly coupled exciton-plasmon systems.

However there are two limitations in the current RT-TDDFT/TD-ωFQ method. First we do not include interband excitations of MNP which is described by the metal polarizability. To do that, we should couple TDKS equation with ωFQFμ model. The extension of ωFQFμ to time-domain may be feasible by adopting the generic dielectric function technique.[30] The second point is that the charge transfer effect between molecule and MNPs is in the absence, which is a nonnegligible effect when the wavefunction of molecule and MNP can effectively overlap.

SUPPLEMENTARY MATERIAL

See the supplementary material for the fitting expression of scaling factor and the validation of the implementation of dissipative propagator.

ACKNOWLEDGMENTS

This work is supported by the National Natural Science Foundation of China (Grant Nos. 22173074, and 21833006).

DATA AVAILABILITY STATEMENT

The data that support the findings of this study are available within the article and its supplementary material. The standalone version of ωFQ source code is available at https://github.com/St-Maxwell/wFQ.

Appendix A: Dissipative TDKS Equation

The Liouville-von Neumann (LvN) equation of TDKS in molecular orbital basis including a phenomenological description of dissipation is given as

$$\frac{\mathrm{d}P'_{pq}}{\mathrm{d}t} = -i[\mathbf{F}'(t), \mathbf{P}'(t)]_{pq} - \gamma_{pq}[P'_{pq}(t) - P'_{pq}(0)], \tag{A1}$$

where γ_{pq} is the damping rate of element $P'_{pq}(t)$. This form of LvN equation includes two processes of the evolution of density matrix. The first part is the ideal evolution

$$\frac{\mathrm{d}P'_{pq}}{\mathrm{d}t} = -i[\mathbf{F}'(t), \mathbf{P}'(t)]_{pq}, \tag{A2}$$

which is usually numerically integrated using the unitary propagator

$$\mathbf{P}_{n+1} = \hat{\mathscr{U}}(t_n, \Delta t)\mathbf{P}_n = \mathbf{U}(t_n, \Delta t)\mathbf{P}_n\mathbf{U}^\dagger(t_n, \Delta t). \tag{A3}$$

In this work, the modified midpoint unitary transformation (MMUT) method[76] is used.

The second part is dissipative, corresponding to the relaxation of $P'_{pq}(t)$ to its equilibrium value $P'_{pq}(0)$

$$\frac{\mathrm{d}P'_{pq}}{\mathrm{d}t} = -\gamma_{pq}[P'_{pq}(t) - P'_{pq}(0)]. \tag{A4}$$

However, there are two problems to be solved before we include the dissipative part in the TDKS. The first aim is to determine the actual value of γ_{pq}. To do so, we review the orbital rotation description of the undamped TDKS. The time-evolution of a single Slater determinant wavefunction can be viewed as orbital rotation acting on the equilibrium wavefunction (i.e. SCF converged wavefunction)[77]

$$\Psi(t) = \mathbf{U}(t)\Psi_0, \tag{A5}$$

where the unitary transform matrix reads

$$\mathbf{U}(t) = \exp\begin{pmatrix} \mathbf{0} & -\Theta^\dagger(t) \\ \Theta(t) & \mathbf{0} \end{pmatrix}. \tag{A6}$$

The orbital rotation parameter matrix $\Theta(t)$ is a complex matrix, and its shape is $N_{\mathrm{vir}} \times N_{\mathrm{occ}}$. Based on $\Theta(t)$, the time-dependent density matrix is

$$\mathbf{P}'(t) = \begin{pmatrix} \cos^2\sqrt{\Theta^\dagger(t)\Theta(t)} & \frac{\sin\left[2\sqrt{\Theta^\dagger(t)\Theta(t)}\right]}{2\sqrt{\Theta^\dagger(t)\Theta(t)}}\Theta^\dagger(t) \\ \Theta(t)\frac{\sin\left[2\sqrt{\Theta^\dagger(t)\Theta(t)}\right]}{2\sqrt{\Theta^\dagger(t)\Theta(t)}} & \sin^2\sqrt{\Theta(t)\Theta^\dagger(t)} \end{pmatrix}. \tag{A7}$$

Here we approximate the expression of $\mathbf{P}'(t)$ up to second-order with respect to $\Theta(t)$

$$\begin{aligned}\mathbf{P}'(t) = &\begin{pmatrix} \mathbf{I}_{\mathrm{oo}} & \mathbf{0} \\ \mathbf{0} & \mathbf{0} \end{pmatrix} + \begin{pmatrix} \mathbf{0} & \Theta^\dagger(t) \\ \Theta(t) & \mathbf{0} \end{pmatrix} \\ &+ \begin{pmatrix} -\Theta^\dagger(t)\Theta(t) & \mathbf{0} \\ \mathbf{0} & \Theta(t)\Theta^\dagger(t) \end{pmatrix} + \mathscr{O}(\Theta^3).\end{aligned} \tag{A8}$$

The above expression is valid as long as the perturbation is not extreme. And in the case of weak field, even the first-order approximation (linear response approximation) is enough. We could assume that the orbital rotation goes back to null exponentially, i.e. we let $\Theta(t)\mathrm{e}^{-\gamma t}$ to replace $\Theta(t)$. Here the decay rate of all elements of $\Theta(t)$ are identical. As a result, the damped time-dependent density matrix should have the following form (up to second-order)

$$\mathbf{P}'(t) = \begin{pmatrix} \mathbf{I}_{\mathrm{oo}} - \Theta^\dagger(t)\Theta(t)\mathrm{e}^{-2\gamma t} & \Theta^\dagger(t)\mathrm{e}^{-\gamma t} \\ \Theta(t)\mathrm{e}^{-\gamma t} & \Theta(t)\Theta^\dagger(t)\mathrm{e}^{-2\gamma t} \end{pmatrix} + \mathscr{O}(\Theta^3). \tag{A9}$$

It is found that the decay rate is 2γ for OO-block and VV-block, and γ for OV-block and VO-block. Then we can conclude that the concrete form of dissipative part should be

$$\frac{\mathrm{d}\mathbf{P}'}{\mathrm{d}t} = \begin{pmatrix} \mathbf{0} & -\gamma \\ -\gamma & \mathbf{0} \end{pmatrix} \cdot [\mathbf{P}'(t) - \mathbf{P}'(0)] \qquad \text{1-order} \tag{A10}$$

$$\frac{\mathrm{d}\mathbf{P}'}{\mathrm{d}t} = \begin{pmatrix} -2\gamma & -\gamma \\ -\gamma & -2\gamma \end{pmatrix} \cdot [\mathbf{P}'(t) - \mathbf{P}'(0)] \qquad \text{2-order} \tag{A11}$$

where the symbol $\cdot$ denotes elementwise multiplication between matrices.

The next issue is the numerical integration method for the TDKS LvN equation after introducing the dissipative part. In this work, we assume that the decay rate of QM molecule is relatively small, that is, weak dissipation. We can adopt operator splitting technique so that the evolution of density matrix for Eq.A1 is[78]

$$\mathbf{P}_{n+1} = \hat{\mathscr{D}}(t_n, \mathrm{d}t/2) \circ \hat{\mathscr{U}}(t_n, \mathrm{d}t) \circ \hat{\mathscr{D}}(t_n, \mathrm{d}t/2)\mathbf{P}_n, \tag{A12}$$

where the symbol $\circ$ denotes operator composition. $\hat{\mathscr{D}}(t_n, \mathrm{d}t)$ is the propagator for Eq. A10 or Eq. A11. The midpoint rule is used to derive the dissipative propagator (take the second-order case as an example)

$$\begin{aligned}\frac{\mathbf{P}'_{n+1} - \mathbf{P}'_n}{\mathrm{d}t} &= \begin{pmatrix} -2\gamma & -\gamma \\ -\gamma & -2\gamma \end{pmatrix} \cdot [\mathbf{P}'(t_n + \mathrm{d}t/2) - \mathbf{P}'(0)] \\ &= \begin{pmatrix} -2\gamma & -\gamma \\ -\gamma & -2\gamma \end{pmatrix} \cdot \left[\frac{1}{2}\mathbf{P}'_{n+1} + \frac{1}{2}\mathbf{P}'_n - \mathbf{P}'(0)\right].\end{aligned} \tag{A13}$$

After simple algebraic derivation, the dissipative propagator for the second-order approximation of density matrix is

$$\begin{aligned}\mathbf{P}_{n+1} &= \hat{\mathscr{D}}(t_n, \mathrm{d}t)\mathbf{P}_n \\ &= \begin{pmatrix} \dfrac{1-\gamma \mathrm{d}t}{1+\gamma \mathrm{d}t} & \dfrac{1-\gamma \mathrm{d}t/2}{1+\gamma \mathrm{d}t/2} \\ \dfrac{1-\gamma \mathrm{d}t/2}{1+\gamma \mathrm{d}t/2} & \dfrac{1-\gamma \mathrm{d}t}{1+\gamma \mathrm{d}t} \end{pmatrix} \cdot \mathbf{P}_n + \begin{pmatrix} \dfrac{2\gamma \mathrm{d}t}{1+\gamma \mathrm{d}t}\mathbf{I}_{\mathrm{oo}} & \mathbf{0} \\ \mathbf{0} & \mathbf{0} \end{pmatrix},\end{aligned} \tag{A14}$$

and for first-order approximation

$$\begin{aligned}\mathbf{P}_{n+1} &= \hat{\mathscr{D}}(t_n, \mathrm{d}t)\mathbf{P}_n \\ &= \begin{pmatrix} \mathbf{0} & \dfrac{1-\gamma \mathrm{d}t/2}{1+\gamma \mathrm{d}t/2} \\ \dfrac{1-\gamma \mathrm{d}t/2}{1+\gamma \mathrm{d}t/2} & \mathbf{0} \end{pmatrix} \cdot \mathbf{P}_n.\end{aligned} \tag{A15}$$

It is worth noting that the propagator $\hat{\mathscr{D}}(t_n, \mathrm{d}t)$ for both cases preserves the trace of density matrix, i.e. the number of electrons.

[1] C. Novo, A. M. Funston, and P. Mulvaney, "Direct observation of chemical reactions on single gold nanocrystals using surface plasmon spectroscopy," Nat. Nanotechnol. **3**, 598–602 (2008).

[2] W. Hou, W. H. Hung, P. Pavaskar, A. Goeppert, M. Aykol, and S. B. Cronin, "Photocatalytic conversion of CO_2 to hydrocarbon fuels via plasmon-enhanced absorption and metallic interband transitions," ACS Catal. **1**, 929–936 (2011).

[3] R. F. Aroca, "Plasmon enhanced spectroscopy," Phys. Chem. Chem. Phys. **15**, 5355–5363 (2013).

[4] C. D. Geddes, "Metal-enhanced fluorescence," Phys. Chem. Chem. Phys. **15**, 19537–19537 (2013).

[5] J. Dong, Z. Zhang, H. Zheng, and M. Sun, "Recent progress on plasmon-enhanced fluorescence," Nanophotonics **4**, 472–490 (2015).

[6] J.-F. Li, C.-Y. Li, and R. F. Aroca, "Plasmon-enhanced fluorescence spectroscopy," Chem. Soc. Rev. **46**, 3962–3979 (2017).

[7] M. J. Kale, T. Avanesian, H. Xin, J. Yan, and P. Christopher, "Controlling catalytic selectivity on metal nanoparticles by direct photoexcitation of adsorbate-metal bonds," Nano Lett. **14**, 5405–5412 (2014).

[8] S. Linic, U. Aslam, C. Boerigter, and M. Morabito, "Photochemical transformations on plasmonic metal nanoparticles," Nat. Mater. **14**, 567–576 (2015).

[9] U. Aslam, V. G. Rao, S. Chavez, and S. Linic, "Catalytic conversion of solar to chemical energy on plasmonic metal nanostructures," Nat. Catal. **1**, 656–665 (2018).

[10] E. Kazuma and Y. Kim, "Mechanistic studies of plasmon chemistry on metal catalysts," Angew. Chem. Int. Ed. **58**, 4800–4808 (2019).

[11] C. Zhan, J. Yi, S. Hu, X.-G. Zhang, D.-Y. Wu, and Z.-Q. Tian, "Plasmon-mediated chemical reactions," Nat. Rev. Methods Primers **3**, 12 (2023).

[12] B. M. Weight, X. Li, and Y. Zhang, "Theory and modeling of light-matter interactions in chemistry: Current and future," Phys. Chem. Chem. Phys. **25**, 31554–31577 (2023).

[13] W. Liang, J. Huang, J. Sun, P. Zhang, and A. Li, "Multiscale modeling and simulation of surface-enhanced spectroscopy and plasmonic photocatalysis," WIREs Comput. Mol. Sci. **13**, e1665 (2023).

[14] J. Mullin, N. Valley, M. G. Blaber, and G. C. Schatz, "Combined quantum mechanics (TDDFT) and classical electrodynamics (Mie theory) methods for calculating surface enhanced Raman and hyper-Raman spectra," J. Phys. Chem. A **116**, 9574–9581 (2012).

[15] W. Yang, G. C. Schatz, and R. P. Van Duyne, "Discrete dipole approximation for calculating extinction and Raman intensities for small particles with arbitrary shapes," J. Chem. Phys. **103**, 869–875 (1995).

[16] H. Chen, J. M. McMahon, M. A. Ratner, and G. C. Schatz, "Classical electrodynamics coupled to quantum mechanics for calculation of molecular optical properties: A RT-TDDFT/FDTD approach," J. Phys. Chem. C **114**, 14384–14392 (2010).

[17] J. Sun, G. Li, and W. Liang, "How does the plasmonic enhancement of molecular absorption depend on the energy gap between molecular excitation and plasmon modes: A mixed TDDFT/FDTD investigation," Phys. Chem. Chem. Phys. **17**, 16835–16845 (2015).

[18] L. Bonatti, G. Gil, T. Giovannini, S. Corni, and C. Cappelli, "Plasmonic resonances of metal nanoparticles: Atomistic vs. continuum approaches," Front. Chem. **8** (2020), 10.3389/fchem.2020.00340.

[19] J. Marcheselli, D. Chateau, F. Lerouge, P. Baldeck, C. Andraud, S. Parola, S. Baroni, S. Corni, M. Garavelli, and I. Rivalta, "Simulating plasmon resonances of gold nanoparticles with bipyramidal shapes by boundary element methods," J. Chem. Theory Comput. **16**, 3807–3815 (2020).

[20] P. Zhang, J. Feist, A. Rubio, P. García-González, and F. J. García-Vidal, "Ab initio nanoplasmonics: The impact of atomic structure," Phys. Rev. B **90**, 161407 (2014).

[21] P. Zhang, W. Jin, and W. Liang, "Size-dependent optical properties of aluminum nanoparticles: From classical to quantum description," J. Phys. Chem. C **122**, 10545–10551 (2018).

[22] J. L. Payton, S. M. Morton, J. E. Moore, and L. Jensen, "A hybrid atomistic electrodynamics-quantum mechanical approach for simulating surface-enhanced Raman scattering," Acc. Chem. Res. **47**, 88–99 (2014).

[23] T. Giovannini, M. Rosa, S. Corni, and C. Cappelli, "A classical picture of subnanometer junctions: An atomistic Drude approach to nanoplasmonics," Nanoscale **11**, 6004–6015 (2019).

[24] P. Lafiosca, T. Giovannini, M. Benzi, and C. Cappelli, "Going beyond the limits of classical atomistic modeling of plasmonic nanostructures," J. Phys. Chem. C **125**, 23848–23863 (2021).

[25] T. Giovannini, L. Bonatti, P. Lafiosca, L. Nicoli, M. Castagnola, P. G. Illobre, S. Corni, and C. Cappelli, "Do we really need quantum mechanics to describe plasmonic properties of metal nanostructures?" ACS Photonics **9**, 3025–3034 (2022).

[26] E. Coccia, J. Fregoni, C. A. Guido, M. Marsili, S. Pipolo, and S. Corni, "Hybrid theoretical models for molecular nanoplasmonics," J. Chem. Phys. **153**, 200901 (2020).

[27] S. Corni, S. Pipolo, and R. Cammi, "Equation of motion for the solvent polarization apparent charges in the polarizable continuum model: Application to real-time TDDFT," J. Phys. Chem. A **119**, 5405–5416 (2015).

[28] S. Pipolo and S. Corni, "Real-time description of the electronic dynamics for a molecule close to a plasmonic nanoparticle," J. Phys. Chem. C **120**, 28774–28781 (2016).

[29] G. Gil, S. Pipolo, A. Delgado, C. A. Rozzi, and S. Corni, "Nonequilibrium solvent polarization effects in real-time electronic dynamics of solute molecules subject to time-dependent electric fields: A new feature of the polarizable continuum model," J. Chem. Theory Comput. **15**, 2306–2319 (2019).

[30] G. Dall'Osto, G. Gil, S. Pipolo, and S. Corni, "Real-time dynamics of plasmonic resonances in nanoparticles described by a boundary element method with generic dielectric function," J. Chem. Phys. **153**, 184114 (2020).

[31] W. Liang, C. T. Chapman, F. Ding, and X. Li, "Modeling ultrafast solvated electronic dynamics using time-dependent density functional theory and polarizable continuum model," J. Phys. Chem. A **116**, 1884–1890 (2012).

[32] P. D. Nguyen, F. Ding, S. A. Fischer, W. Liang, and X. Li, "Solvated first-principles excited-state charge-transfer dynamics with time-dependent polarizable continuum model and solvent dielectric relaxation," J. Phys. Chem. Lett. **3**, 2898–2904 (2012).

[33] F. Ding, D. B. Lingerfelt, B. Mennucci, and X. Li, "Time-dependent non-equilibrium dielectric response in QM/continuum approaches," J. Chem. Phys. **142**, 034120 (2015).

[34] A. Wildman, G. Donati, F. Lipparini, B. Mennucci, and X. Li, "Nonequilibrium environment dynamics in a frequency-dependent polarizable embedding model," J. Chem. Theory Comput. **15**, 43–51 (2019).

[35] X. Wu, J.-M. Teuler, F. Cailliez, C. Clavaguéra, D. R. Salahub, and A. de la Lande, "Simulating electron dynamics in polarizable environments," J. Chem. Theory Comput. **13**, 3985–4002 (2017).

[36] A. Yamada, "Classical electronic and molecular dynamics simulation for optical response of metal system," J. Chem. Phys. **155**, 174118 (2021).

[37] S. M. Morton and L. Jensen, "A discrete interaction model/quantum me-

chanical method for describing response properties of molecules adsorbed on metal nanoparticles," J. Chem. Phys. **133**, 074103 (2010).
[38]S. M. Morton and L. Jensen, "A discrete interaction model/quantum mechanical method to describe the interaction of metal nanoparticles and molecular absorption," J. Chem. Phys. **135**, 134103 (2011).
[39]J. L. Payton, S. M. Morton, J. E. Moore, and L. Jensen, "A discrete interaction model/quantum mechanical method for simulating surface-enhanced Raman spectroscopy," J. Chem. Phys. **136**, 214103 (2012).
[40]Z. Hu, D. V. Chulhai, and L. Jensen, "Simulating surface-enhanced hyper-Raman scattering using atomistic electrodynamics-quantum mechanical models," J. Chem. Theory Comput. **12**, 5968–5978 (2016).
[41]J. C. Becca, X. Chen, and L. Jensen, "A discrete interaction model/quantum mechanical method for simulating surface-enhanced Raman spectroscopy in solution," J. Chem. Phys. **154**, 224705 (2021).
[42]P. Lafiosca, L. Nicoli, L. Bonatti, T. Giovannini, S. Corni, and C. Cappelli, "Qm/classical modeling of surface enhanced Raman scattering based on atomistic electromagnetic models," J. Chem. Theory Comput. **19**, 3616–3633 (2023).
[43]K. Yabana and G. F. Bertsch, "Time-dependent local-density approximation in real time," Phys. Rev. B **54**, 4484 (1996).
[44]A. Castro, M. A. Marques, and A. Rubio, "Propagators for the time-dependent Kohn-Sham equations," J. Chem. Phys. **121**, 3425–3433 (2004).
[45]J. Sun, J. Song, Y. Zhao, and W.-Z. Liang, "Real-time propagation of the reduced one-electron density matrix in atom-centered Gaussian orbitals: Application to absorption spectra of silicon clusters," J. Chem. Phys. **127**, 234107 (2007).
[46]X. Andrade, D. Strubbe, U. De Giovannini, A. H. Larsen, M. J. Oliveira, J. Alberdi-Rodriguez, A. Varas, I. Theophilou, N. Helbig, M. J. Verstraete, *et al.*, "Real-space grids and the Octopus code as tools for the development of new simulation approaches for electronic systems," Phys. Chem. Chem. Phys. **17**, 31371–31396 (2015).
[47]Y. Gao and D. Neuhauser, "Dynamical quantum-electrodynamics embedding: Combining time-dependent density functional theory and the near-field method," J. Chem. Phys. **137**, 074113 (2012).
[48]C. Yam, L. Meng, G. Chen, Q. Chen, and N. Wong, "Multiscale quantum mechanics/electromagnetics simulation for electronic devices," Phys. Chem. Chem. Phys. **13**, 14365–14369 (2011).
[49]J. L. Alonso, X. Andrade, P. Echenique, F. Falceto, D. Prada-Gracia, and A. Rubio, "Efficient formalism for large-scale ab initio molecular dynamics based on time-dependent density functional theory," Phys. Rev. Lett. **101**, 096403 (2008).
[50]C. F. Craig, W. R. Duncan, and O. V. Prezhdo, "Trajectory surface hopping in the time-dependent Kohn-Sham approach for electron-nuclear dynamics," Phys. Rev. Lett. **95**, 163001 (2005).
[51]J. Sun, Z. Ding, Y. Yu, and W. Liang, "Nonlinear features of Fano resonance: A QM/EM study," Phys. Chem. Chem. Phys. **23**, 15994–16004 (2021).
[52]J. Huang, X. Zhao, X. Huang, and W. Liang, "Understanding the mechanism of plasmon-driven water splitting: Hot electron injection and a near field enhancement effect," Phys. Chem. Chem. Phys. **23**, 25629–25636 (2021).
[53]A. Coomar, C. Arntsen, K. A. Lopata, S. Pistinner, and D. Neuhauser, "Near-field: A finite-difference time-dependent method for simulation of electrodynamics on small scales," J. Chem. Phys. **135**, 084121 (2011).
[54]F. Lipparini and V. Barone, "Polarizable force fields and polarizable continuum model: A fluctuating charges/PCM approach. 1. theory and implementation," J. Chem. Theory Comput. **7**, 3711–3724 (2011).
[55]C. Cappelli, "Integrated QM/polarizable MM/continuum approaches to model chiroptical properties of strongly interacting solute–solvent systems," Int. J. Quantum Chem. **116**, 1532–1542 (2016).
[56]T. Giovannini, L. Grazioli, M. Ambrosetti, and C. Cappelli, "Calculation of IR spectra with a fully polarizable QM/MM approach based on fluctuating charges and fluctuating dipoles," J. Chem. Theory Comput. **15**, 5495–5507 (2019).
[57]W. Liang, S. Yokojima, and G. Chen, "Generalized linear-scaling localized-density-matrix method," J. Chem. Phys. **110**, 1844–1855 (1999).
[58]E. Epifanovsky, A. T. B. Gilbert, X. Feng, J. Lee, Y. Mao, N. Mardirossian, P. Pokhilko, A. F. White, M. P. Coons, A. L. Dempwolff, Z. Gan, D. Hait, P. R. Horn, L. D. Jacobson, I. Kaliman, J. Kussmann, A. W. Lange, K. U. Lao, D. S. Levine, J. Liu, S. C. McKenzie, A. F. Morrison, K. D. Nanda, F. Plasser, D. R. Rehn, M. L. Vidal, Z.-Q. You, Y. Zhu, B. Alam, B. J. Albrecht, A. Aldossary, E. Alguire, J. H. Andersen, V. Athavale, D. Barton, K. Begam, A. Behn, N. Bellonzi, Y. A. Bernard, E. J. Berquist, H. G. A. Burton, A. Carreras, K. Carter-Fenk, R. Chakraborty, A. D. Chien, K. D. Closser, V. Cofer-Shabica, S. Dasgupta, M. de Wergifosse, J. Deng, M. Diedenhofen, H. Do, S. Ehlert, P.-T. Fang, S. Fatehi, Q. Feng, T. Friedhoff, J. Gayvert, Q. Ge, G. Gidofalvi, M. Goldey, J. Gomes, C. E. González-Espinoza, S. Gulania, A. O. Gunina, M. W. D. Hanson-Heine, P. H. P. Harbach, A. Hauser, M. F. Herbst, M. Hernández Vera, M. Hodecker, Z. C. Holden, S. Houck, X. Huang, K. Hui, B. C. Huynh, M. Ivanov, A. Jász, H. Ji, H. Jiang, B. Kaduk, S. Kähler, K. Khistyaev, J. Kim, G. Kis, P. Klunzinger, Z. Koczor-Benda, J. H. Koh, D. Kosenkov, L. Koulias, T. Kowalczyk, C. M. Krauter, K. Kue, A. Kunitsa, T. Kus, I. Ladjánszki, A. Landau, K. V. Lawler, D. Lefrancois, S. Lehtola, R. R. Li, Y.-P. Li, J. Liang, M. Liebenthal, H.-H. Lin, Y.-S. Lin, F. Liu, K.-Y. Liu, M. Loipersberger, A. Luenser, A. Manjanath, P. Manohar, E. Mansoor, S. F. Manzer, S.-P. Mao, A. V. Marenich, T. Markovich, S. Mason, S. A. Maurer, P. F. McLaughlin, M. F. S. J. Menger, J.-M. Mewes, S. A. Mewes, P. Morgante, J. W. Mullinax, K. J. Oosterbaan, G. Paran, A. C. Paul, S. K. Paul, F. Pavošević, Z. Pei, S. Prager, E. I. Proynov, A. Rák, E. Ramos-Cordoba, B. Rana, A. E. Rask, A. Rettig, R. M. Richard, F. Rob, E. Rossomme, T. Scheele, M. Scheurer, M. Schneider, N. Sergueev, S. M. Sharada, W. Skomorowski, D. W. Small, C. J. Stein, Y.-C. Su, E. J. Sundstrom, Z. Tao, J. Thirman, G. J. Tornai, T. Tsuchimochi, N. M. Tubman, S. P. Veccham, O. Vydrov, J. Wenzel, J. Witte, A. Yamada, K. Yao, S. Yeganeh, S. R. Yost, A. Zech, I. Y. Zhang, X. Zhang, Y. Zhang, D. Zuev, A. Aspuru-Guzik, A. T. Bell, N. A. Besley, K. B. Bravaya, B. R. Brooks, D. Casanova, J.-D. Chai, S. Coriani, C. J. Cramer, G. Cserey, I. DePrince, A. Eugene, J. DiStasio, Robert A., A. Dreuw, B. D. Dunietz, T. R. Furlani, I. Goddard, William A., S. Hammes-Schiffer, T. Head-Gordon, W. J. Hehre, C.-P. Hsu, T.-C. Jagau, Y. Jung, A. Klamt, J. Kong, D. S. Lambrecht, W. Liang, N. J. Mayhall, C. W. McCurdy, J. B. Neaton, C. Ochsenfeld, J. A. Parkhill, R. Peverati, V. A. Rassolov, Y. Shao, L. V. Slipchenko, T. Stauch, R. P. Steele, J. E. Subotnik, A. J. W. Thom, A. Tkatchenko, D. G. Truhlar, T. Van Voorhis, T. A. Wesolowski, K. B. Whaley, I. Woodcock, H. Lee, P. M. Zimmerman, S. Faraji, P. M. W. Gill, M. Head-Gordon, J. M. Herbert, and A. I. Krylov, "Software for the frontiers of quantum chemistry: An overview of developments in the Q-Chem 5 package," J. Chem. Phys. **155**, 084801 (2021).
[59]Y. Zhu and J. M. Herbert, "Self-consistent predictor/corrector algorithms for stable and efficient integration of the time-dependent Kohn-Sham equation," J. Chem. Phys. **148**, 044117 (2018).
[60]T. S. Nguyen and J. Parkhill, "Nonadiabatic dynamics for electrons at second-order: Real-time TDDFT and OSCF2," J. Chem. Theory Comput. **11**, 2918–2924 (2015).
[61]P.-F. Loos, A. Scemama, M. Boggio-Pasqua, and D. Jacquemin, "Mountaineering strategy to excited states: Highly accurate energies and benchmarks for exotic molecules and radicals," J. Chem. Theory Comput. **16**, 3720–3736 (2020).
[62]P. J. Stephens, F. J. Devlin, C. F. Chabalowski, and M. J. Frisch, "Ab initio calculation of vibrational absorption and circular dichroism spectra using density functional force fields," J. Phys. Chem. **98**, 11623–11627 (1994).
[63]F. Weigend and R. Ahlrichs, "Balanced basis sets of split valence, triple zeta valence and quadruple zeta valence quality for H to Rn: Design and assessment of accuracy," Phys. Chem. Chem. Phys. **7**, 3297 (2005).
[64]A. H. Larsen, J. J. Mortensen, J. Blomqvist, I. E. Castelli, R. Christensen, M. Dułak, J. Friis, M. N. Groves, B. Hammer, C. Hargus, E. D. Hermes, P. C. Jennings, P. B. Jensen, J. Kermode, J. R. Kitchin, E. L. Kolsbjerg, J. Kubal, K. Kaasbjerg, S. Lysgaard, J. B. Maronsson, T. Maxson, T. Olsen, L. Pastewka, A. Peterson, C. Rostgaard, J. Schiøtz, O. Schütt, M. Strange, K. S. Thygesen, T. Vegge, L. Vilhelmsen, M. Walter, Z. Zeng, and K. W. Jacobsen, "The atomic simulation environment–a Python library for working with atoms," J. Phys.: Condens. Matter **29**, 273002 (2017).
[65]D. Rappoport and F. Furche, "Property-optimized Gaussian basis sets for molecular response calculations," J. Chem. Phys. **133**, 134105 (2010).
[66]J.-H. Li, M. Hayashi, and G.-Y. Guo, "Plasmonic excitations in quantum-sized sodium nanoparticles studied by time-dependent density functional calculations," Phys. Rev. B **88**, 155437 (2013).
[67]H. Xiang, X. Zhang, D. Neuhauser, and G. Lu, "Size-dependent plasmonic resonances from large-scale quantum simulations," J. Phys. Chem. Lett. **5**,

1163–1169 (2014).
[68]N. L. Matsko, "Formation of normal surface plasmon modes in small sodium nanoparticles," Phys. Chem. Chem. Phys. **22**, 13285–13291 (2020).
[69]L. Novotny and B. Hecht, *Principles of Nano-Optics*, 2nd ed. (Cambridge University Press, 2012).
[70]S. Corni and J. Tomasi, "Excitation energies of a molecule close to a metal surface," J. Chem. Phys. **117**, 7266–7278 (2002).
[71]S. Corni and J. Tomasi, "Lifetimes of electronic excited states of a molecule close to a metal surface," J. Chem. Phys. **118**, 6481–6494 (2003).
[72]O. Andreussi, S. Corni, B. Mennucci, and J. Tomasi, "Radiative and nonradiative decay rates of a molecule close to a metal particle of complex shape," J. Chem. Phys. **121**, 10190–10202 (2004).
[73]C. Ott, A. Kaldun, P. Raith, K. Meyer, M. Laux, J. Evers, C. H. Keitel, C. H. Greene, and T. Pfeifer, "Lorentz meets Fano in spectral line shapes: A universal phase and its laser control," Science **340**, 716–720 (2013).
[74]Y. S. Joe, A. M. Satanin, and C. S. Kim, "Classical analogy of Fano resonances," Phys. Scr. **74**, 259 (2006).
[75]B. Zhang and W. Liang, "The vibronic absorption spectra and exciton dynamics of plasmon-exciton hybrid systems in the regimes ranged from Fano antiresonance to Rabi-like splitting," J. Chem. Phys. **152**, 014102 (2020).
[76]X. Li, S. M. Smith, A. N. Markevitch, D. A. Romanov, R. J. Levis, and H. B. Schlegel, "A time-dependent Hartree–Fock approach for studying the electronic optical response of molecules in intense fields," Phys. Chem. Chem. Phys. **7**, 233–239 (2005).
[77]J. Yang, Z. Pei, J. Deng, Y. Mao, Q. Wu, Z. Yang, B. Wang, C. M. Aikens, W. Liang, and Y. Shao, "Analysis and visualization of energy densities. i. insights from real-time time-dependent density functional theory simulations," Phys. Chem. Chem. Phys. **22**, 26838–26851 (2020).
[78]B. A. Shadwick and W. F. Buell, "Unitary integration with operator splitting for weakly dissipative systems," J. Phys. A Math. Gen. **34**, 4771 (2001).